ELSEVIER

Ceramics International 31 (2005) 703–711

CERAMICS INTERNATIONAL

www.elsevier.com/locate/ceramint

Gas pressure sintering of SiC sintered with rare-earth-(III)-oxides and their mechanical properties

Koushik Biswas[a,b,*], Georg Rixecker[b], Fritz Aldinger[b]

[a]*Department of Metallurgical and Materials Engineering, Indian Institute of Technology, Kharagpur 721302, India*
[b]*Max-Planck Institut für Metallforschung and Institut für Nichtmetallische Anorganische Materialien, Universität Stuttgart, Pulvermetallurgisches Laboratorium, Heisenbergstraße 3, 70569 Stuttgart, Germany*

Received 7 January 2004; received in revised form 27 February 2004; accepted 25 June 2004
Available online 17 February 2005

Abstract

The sintering behaviour of LPS-SiC and the influence of the size of the rare-earth cations on the secondary phase characteristics were investigated with different rare-earth oxide additions. In all cases, the most important sintering mechanism was found to be the solution-reprecipitation process. This fact was corroborated by TEM and EDS analyses. Post-sintering annealing resulted in devitrification of the secondary phases coupled with anisotropic grain growth due to the phase transformation from β-SiC to α-SiC. Improved fracture toughness of the annealed materials was attributed to crack deflection by the elongated grains. SEM microstructural analyses were performed in order to elucidate structure–property relationships. A comparative study in reference to the additive system Y_2O_3–AlN demonstrates significantly improved high-temperature properties of the Lu_2O_3-containing SiC ceramics.

Keywords: A. Sintering; C. Strength; D. SiC; Rare-earth oxides; Fracture toughness

1. Introduction

Silicon carbide is a potentially important material for high-temperature structural components because of its unique combination of properties, such as excellent oxidation resistance, high-temperature strength retention, high wear resistance, good thermal conductivity and thermal shock resistance. However, it is difficult to densify without additives because of the covalent nature of Si–C bond and the low self diffusion coefficients [1]. Prochazka [2], in his pioneering work, developed a pressureless sintering method leading to good sinterability of silicon carbide powder with additions of boron and carbon. Later on, combined additions of boron, aluminium, carbon or their compounds were successfully used as sintering aids to fabricate SiC ceramics [3–9].

An innovative approach of using liquid-phase sintering for the densification of SiC was introduced by Omori and Takei [10–12] in the 1980s. They investigated several oxide systems and showed that oxide additives do promote the densification of SiC via a liquid phase. During last decade, additive systems such as Al_2O_3–Y_2O_3 and AlN–Y_2O_3 were extensively used to obtain dense LPS-SiC ceramics [13–20]. However, it was established that the densification aids invariably form ''weak'' grain-boundary phases [13,14] affecting the final high-temperature properties.

In order to improve the thermo-mechanical properites, several rare-earth oxides were introduced in recent years as densification additives for Si_3N_4 and SiAlON ceramics [21–26]. These new rare-earth oxide additive systems were introduced for the modification of the grain boundaries by highly refractory crystalline rare-earth disilicates ($R_2Si_2O_7$) leading to improved high-temperature properties. Moreover, it has been observed that the solubility of N in oxynitride glasses containing rare-earth oxides can reach higher levels as compared to conventional additive systems [27].

* Corresponding author.

0272-8842/$30.00
doi:10.1016/j.ceramint.2004.06.027

The glass transition temperatures and softening points of oxynitride glasses are significantly higher than those of silicate glasses [28], contributing to superior high-temperature properties of the sintered ceramics.

The present sintering study is a contribution towards the understanding of the sintering behaviour of LPS-SiC with different combinations of rare-earth oxides. In this case, the melting point depression in the R_2O_3–R'_2O_3 systems at intermediate composition is exploited for the formation of a liquid phase. Out of large number of additive systems investigated (R = Nd, Gd, Dy, Y, Ho and R = Ho, Er, Lu) [29], the combinations of R = Gd, Dy and R′ = Ho were selected for the present study based on the sinterability of 50:50 (molar ratio) compositions to near theoretical density by means of gas pressure sintering at 2000 °C. The prevailing sintering mechanism in this study was found to be classical liquid phase sintering with solution-reprecipitation of SiC which was corroborated by the TEM and EDS investigations. Microstructural development and phase evolution after sintering and annealing were investigated with the help of SEM and XRD. Anisotropic grain growth behaviour coupled with the β-SiC → α-SiC transformation was correlated with the fracture mechanical properties. In a separate study, LPS-SiC with conventional Y_2O_3–AlN and new rare-earth additive system Lu_2O_3–AlN were compared in terms of mechanical behaviour at room and high temperatures.

2. Experimental procedure

Commercially available α-SiC, β-SiC and R_2O_3 (R = Gd, Ho, Dy, Y, Lu) and AlN powders were used as starting materials. The characteristics of these powders are summarized in Table 1. Powder mixtures were prepared by attrition milling for 4 h in isopropanol with Si_3N_4 milling media using a polyamide container and keeping a ball-to-charge weight ratio of 6:1. After drying and granulation by sieving with a mesh width of 160 μm, the processed powders were cold isostatically pressed at 240 MPa. The compositions of the powder premixes are given in Table 2.

Sintering was performed in a graphite-heated gas pressure furnace (FCT, Germany) at 2000 °C for 1 h. The first stage of sintering was carried out under a slight N_2 overpressure of 0.2 MPa for 30 min, followed by a pressure sintering cycle of 30 min at the same temperature under 10 MPa N_2 to achieve complete densification. Annealing schedules were performed in the same graphite furnace at 1950 °C for different times to effect the β → α-SiC phase transformation. The heating and cooling rates were kept fixed at 10 °C/min.

Table 2
Compositions of powder premixes

Designation	β-SiC:α-SiC (mol%)	Additive A:B (mol%)
1Gd–1Ho	90:10	$50Gd_2O_3$:$50Ho_2O_3$
1Dy–1Ho	90:10	$50Dy_2O_3$:$50Ho_2O_3$
Y–AlN	90:10	$40Y_2O_3$:60AlN[a]
Lu–AlN	90:10	$50Lu_2O_3$:50AlN

[a] Optimized composition in Y_2O_3–AlN system.

X-ray powder diffractometry (XRD) was performed with a Siemens D5000 X-ray diffractometer using filtered Cu Kα radiation with a wavelength of λ = 1.5406 Å. The X-ray diffraction patterns were analysed by using Siemens DIFFRAC-AT software for identifying the phases present and for quantifying the extent of β → α-SiC conversion. The percentage of α-SiC formed upon annealing is calculated from the ratio of the relative intensities of the (1 0 1) reflection of the α-SiC polytype 6H (F) and the SiC reflection with maximum intensity (F_{max}), followed by comparison of that ratio with a calibration curve established by Nader [30].

For scanning electron microscopy (SEM) observations, the specimens were ground and polished to 1 μm surface finish. After polishing, the samples were plasma etched using a RF Plasma Barrel Etcher (Biorad PT7150) for 3–3.5 min in a mixture of CF_4 and O_2 at 1:1 ratio. Microstructures of the sintered and annealed specimens were examined with scanning electron microscopes of types S200, Cambridge Instruments, and DSM 982 GEMINI, Leo. Grain sizes and aspect ratios were calculated using an image analysis software (Imtronic, Germany). The sintered samples were cut, thinned and investigated using energy filtered transmision electron microscope (EFTEM) having a maximum accelerating voltage of 120 keV (Zeiss EM 912 Omega). This instrument was also used for energy dispersive microanalysis (EDS).

Table 1
Characteristics of the starting powders

Powder	Designation manufacturer	Chemical analysis (wt.%)	Particle size distribution			Specific area (m^2/g)	Density (g/cm^3)
			d_{10} (μm)	d_{50} (μm)	d_{90} (μm)		
α-SiC	A-10 H.C. Starck, Germany	C-30.0, O-0.9, Al-0.03, Ca-0.01, Fe-0.05	0.18	0.51	1.43	11.1	3.22
β-SiC	BF-12 H.C. Starck, Germany	C-30.0, O-1.2, Al-0.05, Ca-0.005, Fe-0.03	0.25	0.89	3.50	17.8	3.22
AlN	Grade C, H.C. Starck	N-30.0, C-0.1, O-2.5, Fe-0.005	0.34	0.92	3.07	5.0	3.26
Y_2O_3	Grade C, H.C. Starck	Al-0.005, Ca-0.003, Fe-0.005	1.21	4.48	8.08	12.9	5.02
Gd_2O_3	STREM CHEMICALS USA	99.99% Gd		∼1 to 2 μm		–	7.41
Dy_2O_3	STREM CHEMICALS USA	99.90% Dy		<65 μm		–	7.81
Ho_2O_3	Alfa Aesar, Germany	99.99% Ho		4–5 μm		–	8.36
Lu_2O_3	STREM CHEMICALS USA	99.90% Lu	–			–	9.45

The fracture toughness of sintered and annealed samples was determined by using the Vickers indentation method. The samples were polished to a surface finish of l μm. For each specimen, 12 indentations are made by a Vickers hardness tester (Buehler Micromet 1) with a load of 5 kg at a constant loading speed of 70 μm/s and a loading time of 15 s. After measuring the crack length and diagonals of the indentation, the fracture toughness was calculated using the following formula [31]:

$$K_{\mathrm{Ic}} = 0.016\sqrt{\frac{E}{H}}FL^{-(3/2)} \quad (1)$$

where E is Young's modulus, taken as 400 GPa for SiC ceramics, H is Vickers hardness (GPa), F = load (N), L is crack length (μm).

The hardness (H) is calculated by the formula [32]:

$$H = 1.8544\left(\frac{F}{d_H^2}\right) \quad (2)$$

where d_H = diagonals of Vickers indentation (μm).

Room and high-temperature bend tests (four-point) were performed in air on test specimens with dimensions: 3 mm × 4 mm × 50 mm, using a universal testing machine (Zwick, Germany) with a fixture of inner and outer span of 20 and 40 mm, respectively. The tensile surface of the bars was polished to 3 μm diamond finish and the tensile edges beveled to avoid stress concentrations and large edge flaws caused by sectioning. The crosshead speed for bending tests was kept at 0.1 mm/s. The stress (σ_{4P}), is calculated assuming elastic response to the imposed bending moment, is given by equation

$$\sigma_{4P} = \frac{3}{2}\left(\frac{F(l_o - l_i)}{bh^2}\right) \quad (3)$$

where σ_{4P} is four-point bending strength (MPa), F is force (N), l_o and l_i are the respective lengths between the two outer (40 mm) and inner supports (20 mm), b and h are breadth and height of the specimen, respectively.

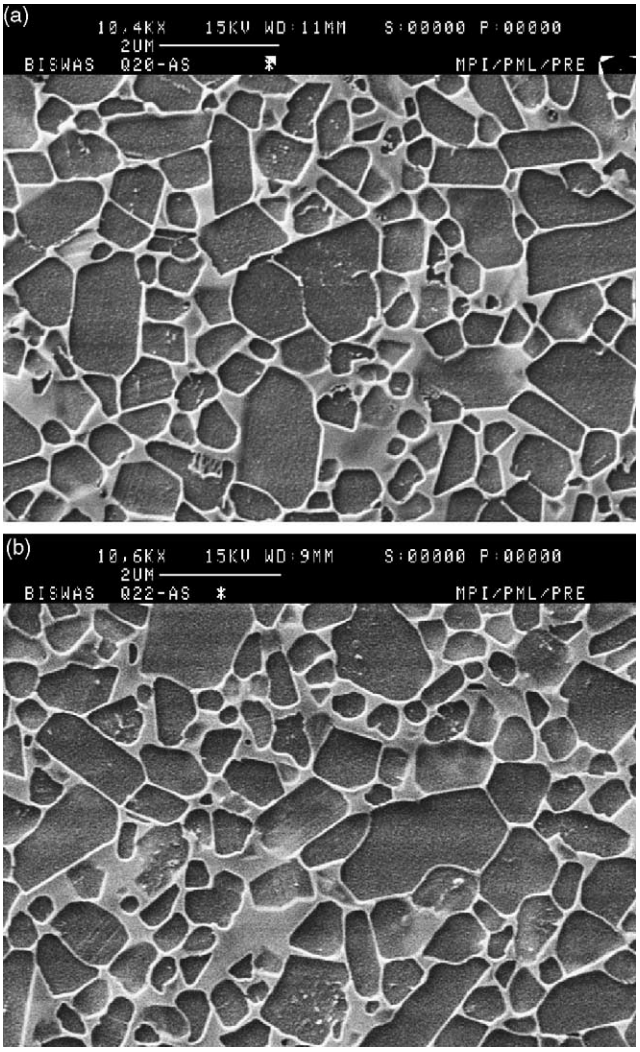

Fig. 1. Microstructure of as-sintered SiC materials gas-pressured sintered in N_2: (a) 1Gd–1Ho and (b) 1Dy–1Ho.

3. Results and discussion

3.1. LPS-SiC with R_2O_3–R'_2O_3 systems

3.1.1. Sintering behaviour

During sintering, complete wettability of the SiC grains and a homogeneous microstructure are obtained in both systems (Fig. 1). The sintered densities of the LPS-SiC with rare-earth oxides are found to be ≥99.5% of the theoretical density as calculated by the rule of mixtures. The sintering mechanism in the 1Gd–1Ho and 1Dy–1Ho systems is not clear from the microstructural observations by SEM (Fig. 1). There is no visible core-rim structure of the SiC grains [33] even after severe plasma etching. However, EDS analysis shows (Fig. 2) traces of oxygen inside the SiC grains which suggests that sintering occurred through the solution-reprecipitation mechanism [34]. This fact is also established by the TEM investigation where the intergranular phases are seen in bright contrast and SiC grains in dark contrast (Fig. 3). The small grain surrounded by intergranular phases is the result of solution-reprecipitation process. During sintering, the mass transport mainly occurs through the liquid phase formed by the dissolution of the two rare-earth oxides along with some amount of SiO_2 present on the surface of the SiC grains. As sintering progresses, SiC grains with highly convex curvature (small grains) will begin to dissolve in the oxide melt to the solubility limit. Initial α-SiC seeds or larger grains act as nucleation sites for α-SiC precipitation. Thus, solution-reprecipitation is expected to occur on the pre-existing α-SiC and is connected with some chemical inhomogenity of the SiC-grains.

EDS analysis of TEM specimens shows some segregation of rare-earth elements depending on their cationic radius. In the 1Dy–1Ho system, the element with higher cationic radius (Dy^{3+}) segregates at intergranular films whereas the

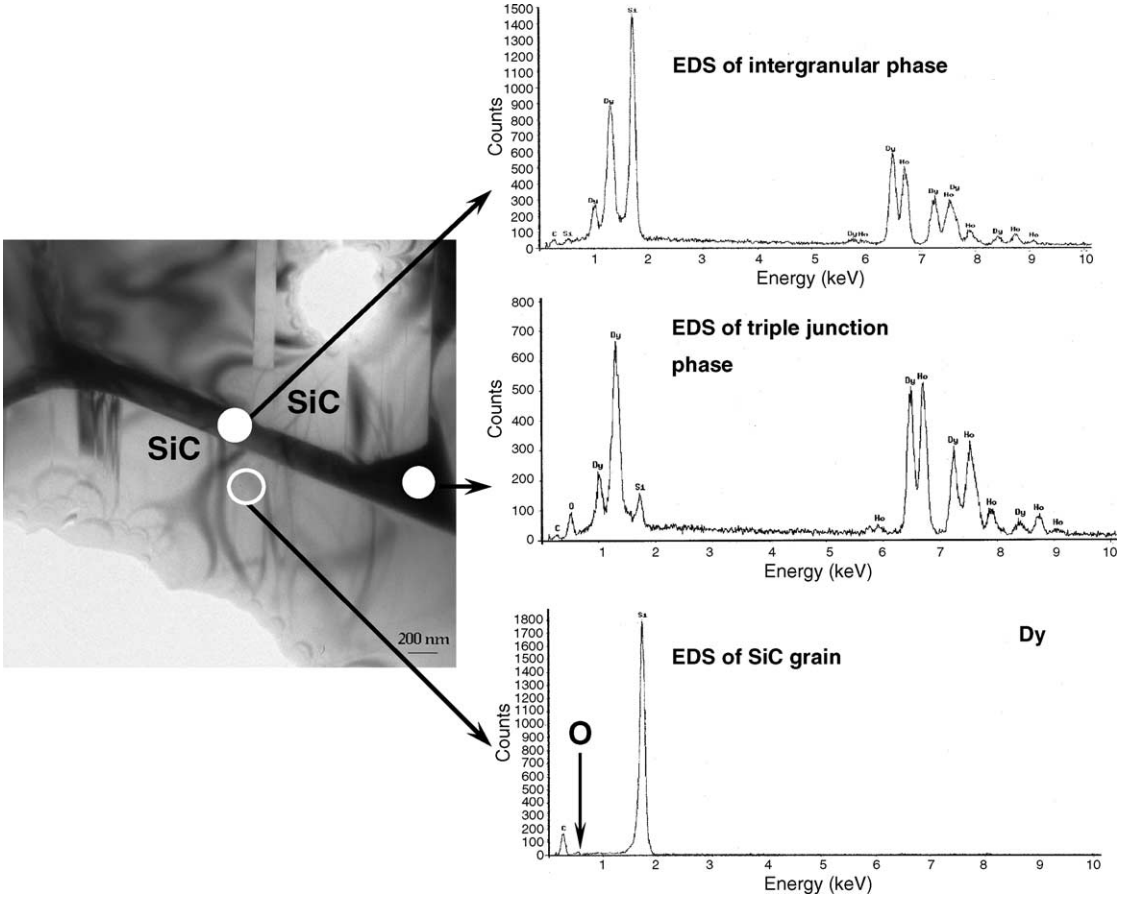

Fig. 2. TEM-EDS analysis of SiC sintered with 1Dy–1Ho showing different spectra obtained from the SiC grain and the intergranular and triple point phases.

content of the element with lower atomic radius (Ho^{3+}) is found to be higher at triple points (Fig. 2). The apparent difference in the Si contents of the intergranular and the triple point regions is due to interference from the neighbouring SiC grains in the topmost spectrum of Fig. 2. For SiAlON ceramics sintered with rare-earth oxides, a similar segregation effect depending on the atomic radius was observed by Rosenflanz and Chen [35].

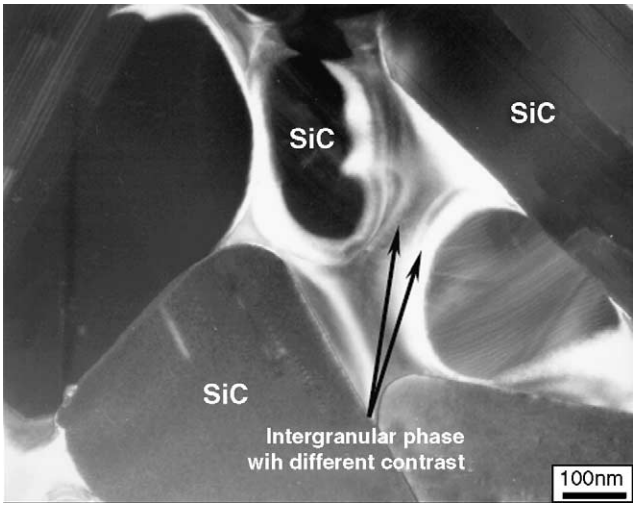

Fig. 3. Dark-field TEM image of SiC sample, where the intergranular phases are seen in bright contrast and SiC grains in dark contrast. The small grain surrounded by intergranular phases is the result of solution-reprecipitation process. The contrast difference caused by this sintering mechanism is clearly visible.

3.1.2. Microstructure and phase evolution

Typical microstructures of LPS-SiC sintered with 1Gd–1Ho and 1Dy–1Ho are shown in Fig. 1. The remnant of the liquid phase is primarily located at the triple or multi-grain junctions. Plasma etching reveals a grain-boundary film present between the SiC grains in both the systems. In order to confirm this, a TEM investigation was performed on these systems. Fig. 4 presents a set of low magnification transmission electron micrographs showing general morphologies of the 1Dy–1Ho system with the SiC grains being in bright contrast. The secondary phases appear in dark contrast because of the presence of the heavy rare-earth elements resulting in high electron scattering. The TEM images, along with electron diffraction patterns (Fig. 4), confirm the presence of partially amorphous intergranular phases along the SiC grain-boundaries as well as at heterophase boundaries (between SiC and crystalline intergranular phases, not shown here). The grain-boundary film in Fig. 4 is unusually wide (∼200 nm). The electron diffraction pattern from the intergranular phase (Fig. 4, part 1) shows spots in addition to annular ring, suggesting that

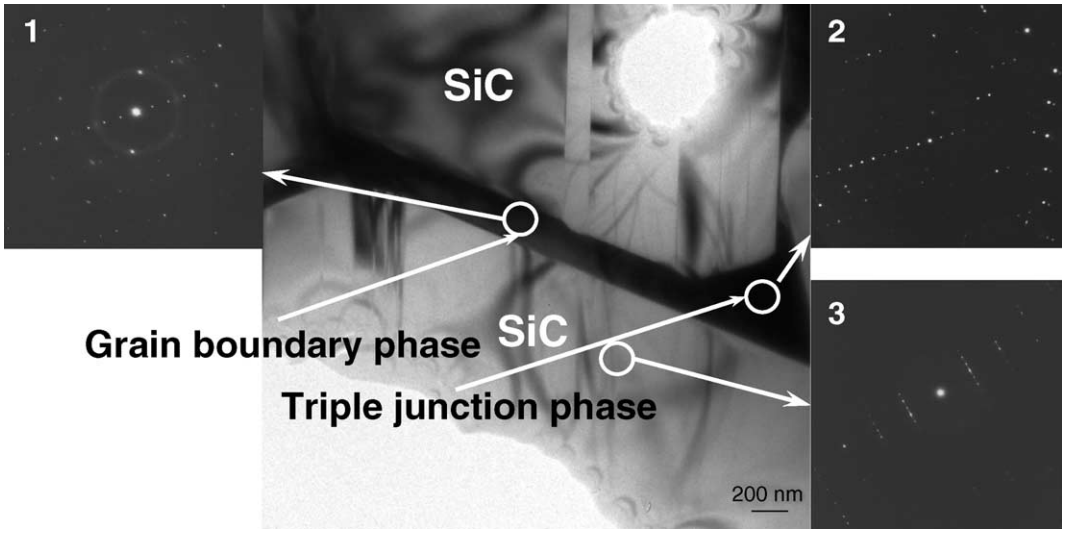

Fig. 4. Transmission electron micrographs along with electron diffraction patterns showing amorphous and crystalline regions in LPS-SiC sintered with 1Dy–1Ho additive system.

partially crystalline phases are present as well. This is different from the observations by Ye [36] on LPS-SiC sintered with AlN–Y_2O_3 additives, where the intergranular films (thickness ∼1 nm) were always amorphous. Triple junction phases are entirely crystalline after sintering as can be seen from the diffraction patterns of triple points (Fig. 4, part 2). According to the XRD pattern of as sintered samples (indicated by ''0 h'') in Fig. 5, the majority of intergranular phases are crystalline in both the 1Gd–1Ho and 1Dy–1Ho, systems showing sharp reflections in the XRD pattern. Little diffuse scattering in the electron diffraction pattern indicates that the amount of residual amorphous phases is small.

Annealing of the SiC materials sintered with the additive systems 1Gd–1Ho and 1Dy–1Ho also gives rise to a plate-like microstructure (Fig. 6), very similar to LPS-SiC sintered with conventional additive systems [30,37,38]. The microstructure changes from equiaxed to platelike grains during annealing, and grain growth proceeds predominantly along the basal plane of the hexagonal crystal lattice (plate-like growth). This anisotropic grain growth of α-SiC grains is related to the β → α-phase transformation and continues until full transformation is achieved or until there is steric hindrance by the neighbouring grains [19,30]. This microstructural development is analogous to the formation of rodlike grains in Si_3N_4-ceramics [16,19,39]. Image analysis of the two dimensional sections provides a rough estimation of the average grain size (measuring the sectional length of the grains), aspect ratio and the secondary phase content in the two systems. These data are tabulated in Table 3.

It is observed that the average grain size increases with annealing along with the aspect ratio, the platelet type of morphology evolving in both systems. However, due to faster kinetics in the system 1Dy–1Ho, the growth of platelet grains is faster. In both cases, secondary phases are expelled from the grain-boundary region and very small amounts of residual secondary phases remain at the triple or multi-grain junctions. The reduction of the residual secondary phases occurs due to the volatilisation of these phases via carbothermal reductions (graphite-heated furnace) [40]. Remarkably, this does not seem to generate any porosity in the present systems. From the micrographs (Figs. 1 and 6) and the phase-transformation plot (Fig. 7), it is clear that the kinetics of the β → α-SiC transformation is somewhat faster in case of the smaller cation contrary to what would expected from chemical considera-

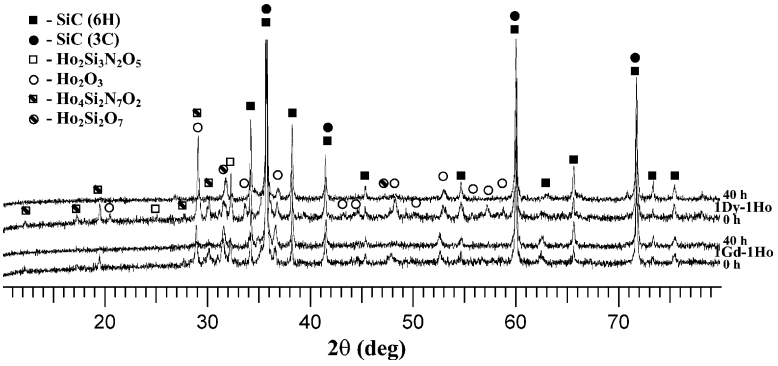

Fig. 5. X-ray diffraction pattern of LPS-SiC sintered with 1Gd–1Ho and 1Dy–1Ho after sintering and annealing for 40 h.

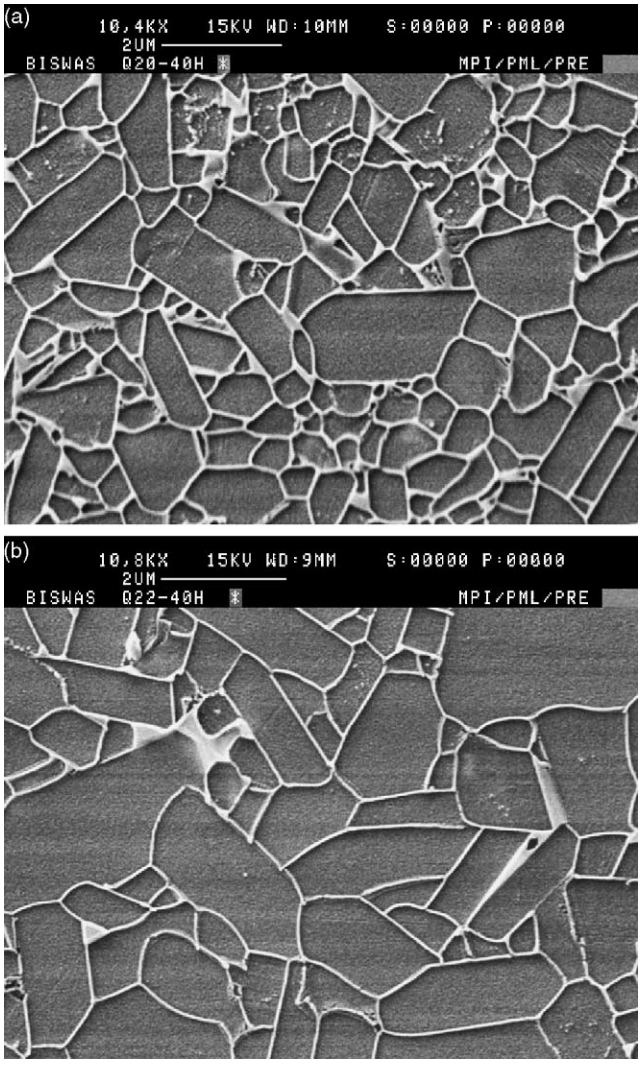

Fig. 6. Microstructure of annealed SiC materials sintered with (a) 1Gd–1Ho and (b) 1Dy–1Ho (compared to Fig. 1).

tions [41]. Although silicate liquids containing larger cations show a lower viscosity (due to lower field strength), the transformation kinetics observed here do not follow this rule. Since material transport through the melt is obviously not the rate-limiting step (otherwise grain growth and transformation would scale with the melt viscosity), the dissolution rate of SiC in the melt is probably rate-determining [20] (or the re-precipitation rate, but this has not yet been reported in connection with this kind of materials). Possibly, the higher field strength of the Dy^{3+} ions makes the 1Dy–1Ho melt more efficient in dissolving SiC.

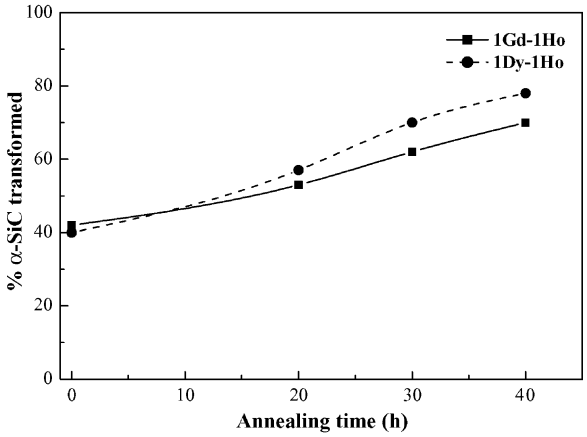

Fig. 7. β → α-SiC phase transformation as a function of annealing time.

3.1.3. Fracture toughness and hardness

Vickers indentation fracture toughness and hardness were measured on as-sintered and annealed samples and are plotted in Fig. 8. In as-sintered samples, cracks propagate mainly along the grain boundaries as the grain-boundary phases are weakened by probable thermal expansion mismatch between them and the SiC grains [42]. However, the crack path remains almost straight as there is no appreciable crack deflection by the fine globular microstructure (Fig. 9a and c). The fracture toughness increases with annealing time for both systems. In the annealed samples, cracks also propagate along the grain boundaries but are continuously deflected by elongated grains (Fig. 9b and d). Crack deflection along the grain boundaries seems to be the main toughening mechanism [43]. Apart from crack deflection, crack bridging, mechanical interlocking and thermally induced microcracking may also play a significant role in the toughening of LPS-SiC ceramics [36,44]. In the present case, the fracture toughness improves with post-sintering annealing treatments, this behaviour being more pronounced in the case of the 1Dy–1Ho additive system as compared to the 1Gd–1Ho system (Fig. 8). This larger improvement of K_{Ic} upon annealing can be directly correlated with the larger grain size and higher aspect ratio.

The Vickers hardness (H) initially remains unchanged for both systems. Thereafter it increases to a maximum value after 30 h of annealing, followed by a drop at the maximum annealing time of 40 h. During annealing, the average grain size ($\bar{G}$) increases in both systems and hence invoking a

Table 3
The average grain size, aspect ratio and the liquid-phase content in sintered and annealed materials after sintering with 1Gd–1Ho and 1Dy–1Ho additive systems

Sample designation	Average grain size (μm) after		Average aspect ratio after		Secondary phase content (%) after	
	Sintering	40 h of annealing	Sintering	40 h of annealing	Sintering	40 h of annealing
1Gd–1Ho	1.0 ± 0.6	1.3 ± 0.7	1.2 ± 0.2	1.6 ± 0.6	11 ± 0.5	2.7 ± 0.3
1Dy–1Ho	1.1 ± 0.5	1.7 ± 0.5	1.3 ± 0.3	2.2 ± 0.5	11 ± 0.4	2.2 ± 0.3

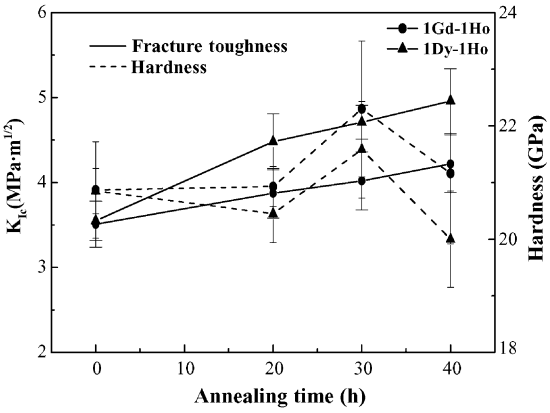

Fig. 8. Variation of fracture toughness and hardness as a function of annealing time in SiC ceramics sintered with 1Gd–1Ho and 1Dy–1Ho additive systems.

Hall-Petch like H versus $\tilde{G}^{-(1/2)}$-behaviour, one can expect a decrease in hardness with increasing average grain size [45]. However, in poly-crystalline materials containing glassy grain-boundary and intergranular phases, after thermal treatment, reduction and re-distribution of the secondary phases generally improve the hardness of the material [40]. In the present case, the glassy phase removal seems to provide the dominant contribution. However, the hardness values drop again after extended annealing. This is thought to be due to the formation of micro-cracking caused by residual stresses generated after considerable grain-boundary phase removal [40]. For 1Dy–1Ho, a higher hardness could be expected due to the lower cationic radius and stronger R–O bond strength, counteracting the micro-structural mechanism described above. This is obviously not the case (Fig. 8).

3.2. LPS-SiC with R_2O_3–AlN systems

3.2.1. Sintering behaviour

Fig. 10 shows microstructures of the SiC ceramics sintered with Y_2O_3–AlN and Lu_2O_3–AlN compositions. Plasma etched samples reveal a typical core and rim structure inside the SiC grains which indicates that the sintering mechanism in these systems is also solution-reprecipitation [34]. Both the core and rim zones consist predominantly of one single polytype of SiC, namely 6H α-SiC. The difference in contrast comes from the differential etching behaviour of the core with respect to the rim region which contains impurities due to the reprecipitation process. This observation corroborates that the sintering proceeds through solution-reprecipitation processes similar to the R_2O_3–R_2O_3 systems discussed in the previous section.

3.2.2. Mechanical properties

Fig. 11 shows the bending strength variation between RT and 1500 °C. An increasing trend is observed till 1200 °C followed by a rather moderate drop in the strength values in case of Lu–AlN samples. However, this rise is more pronounced at 1400 °C in case of SiC with Y–AlN additive system. The increase in flexural strength corresponds to flaw and surface crack healing due to oxidation [17]. Apart from that, surface compressive stress due to oxidation of oxynitride phases is also thought to reinforce the material [20]. This effect is more predominant in case of Y–AlN as the vol.% nitride phase present in the system is higher than that of Lu–AlN system. At higher temperature, the grain-boundary glass phase weakens due to softening. Hence, non-uniform

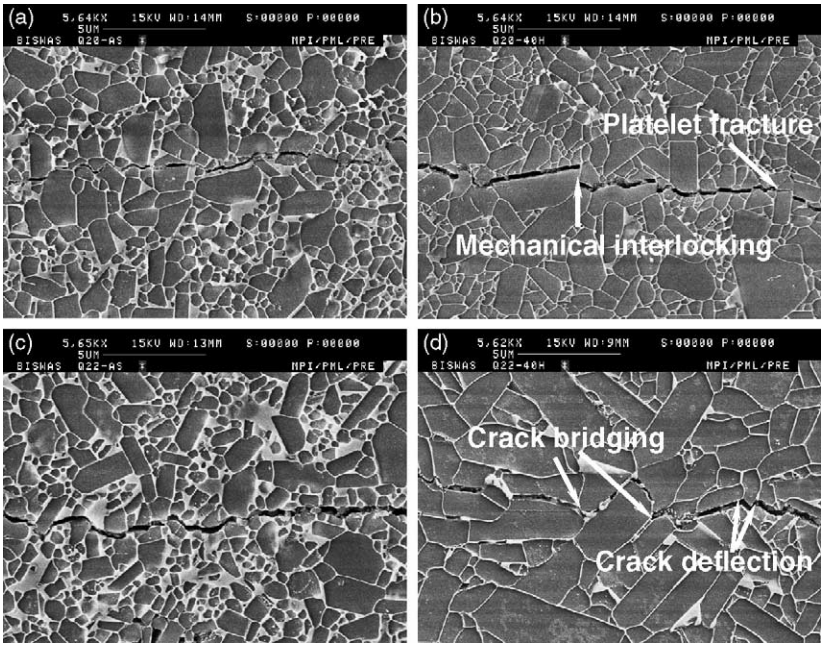

Fig. 9. Vickers indentation crack propagation in as sintered (a) 1Gd–1Ho and (c) 1Dy–1Ho and in annealed (for 40 h) (b) 1Gd–1Ho and (d) 1Dy–1Ho.

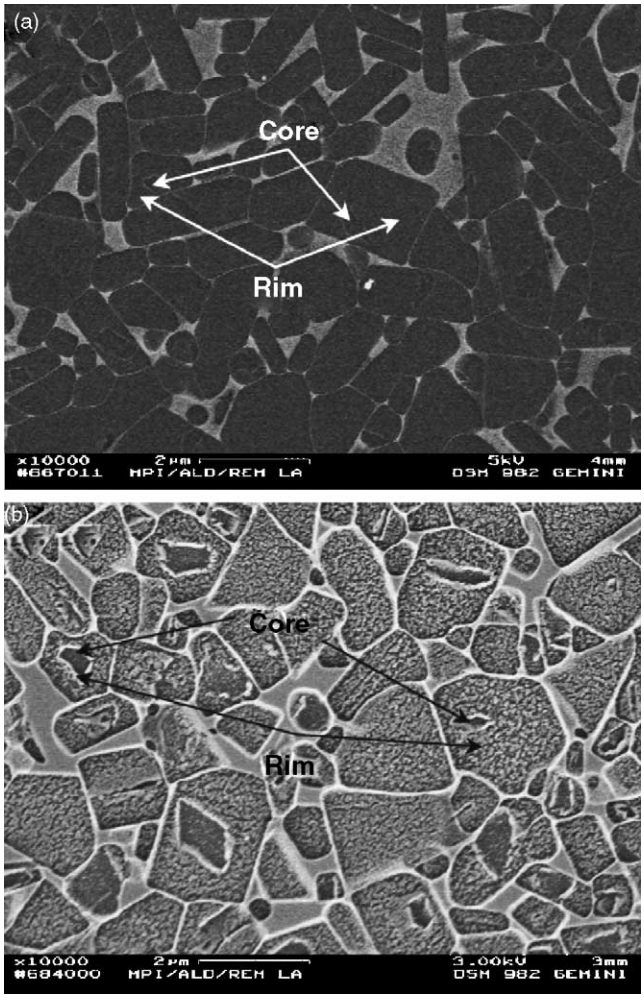

Fig. 10. Microstructure of LPS-SiC ceramic sintered with (a) Y–AlN and (b) Lu–AlN additives.

deformation such as grain-boundary sliding (grain-boundary glass flow) occurs and the stress concentration at crystallised triple junctions increases resulting in a drop of the flexural strength [46].

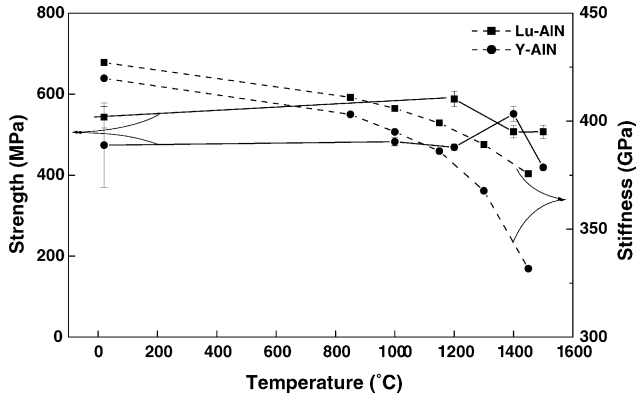

Fig. 11. A comparison of high-temperature strength and stiffness retention for LPS-SiC showing the improved thermo-mechanical properties of the Lu_2O_3–AlN additive system as compared to the "conventional" Y_2O_3–AlN additive.

In order to understand the degradation of the elastic properties, stiffness values have been calculated from the slope of the loading–unloading curve. The stiffness, calculated from the slope of the loading–unloading curve, essentially characterises the elastic and fast recoverable anelastic components of the material's behaviour. It is evident from the Fig. 11 that high-temperature stiffness as well as plastic-anelastic deformation behaviour is improved by the substitution of Y_2O_3 by Lu_2O_3. The deformation associated with viscous flow is diminished because of the more refractory nature of the grain-boundary phase in the system Lu_2O_3–AlN as compared to the Y_2O_3–AlN additive system.

4. Conclusions

β-SiC, seeded with α-SiC, was successfully sintered to full density with Gd_2O_3–Ho_2O_3, Dy_2O_3–Ho_2O_3, Y_2O_3–AlN and Lu_2O_3–AlN additives. More than 99.5% densification were achieved in all of these systems when sintering was carried out in N_2 atmosphere.

Sintering proceeds through the classical solution-reprecipitation mechanism as established by SEM, TEM and EDS analysis. The LPS-SiC sintered with additive systems Gd_2O_3–Ho_2O_3 and Dy_2O_3–Ho_2O_3 have a fine-grained homogeneous microstructure of more or less equiaxed SiC grains which can be suitably designed through post-sintering heat-treatments. Characteristically, the β → α-SiC phase transformation leads to anisotropic grain growth of α-SiC grains which then form an interlocked platelet type of microstructure.

Room temperature fracture toughness and hardness are directly correlated with the microstructure. Improvements in fracture toughness after annealing treatments are due to crack deflection, crack bridging and mechanical interlocking mechanisms.

Excellent thermo-mechanical properties are obtained by the addition of Lu_2O_3, as compared to other rare-earth oxides such as Y_2O_3.

Acknowledgements

The authors would like to thank the technical staff at the Max-Planck Institut für Metallforschung for performing the SEM, TEM, EDS, XRD and strength measurements.

References

[1] C. Greskovich, J.H. Rosolowski, J. Am. Ceram. Soc. 59 (1976) 336.
[2] S. Prochazka, in: A.R. Cooper, A.H. Heuer (Eds.), Mass Transport Phenomena in Ceramics, vol. 9, Plenum Press, New York, 1975, p. 421.
[3] H. Hausner, Energy and ceramics, in: P. Vincenzini (Ed.), Material Science Monographs, vol. 6, Elsevier Scientific Publ. Co., Amsterdam, 1980, p. 582.

[4] H. Suzuki, T. Hase, in: S. Sāmiya, S. Saito (Eds.), Proc. Int. Symp. on Factors in Densification and Sintering of Oxide and Non-Oxide Ceramics, Gakujutsu Bunken, Fukyu-kai, Tokyo, 1979, p. 345.
[5] Y. Murata, R.H. Smoak, in: S. Sāmiya, S. Saito (Eds.), Proc. Int. Symp. on Factors in Densification and Sintering of Oxide and Non-Oxide Ceramics, Gakujutsu Bunken, Fukyu-kai, Tokyo, 1979, p. 383.
[6] D.H. Stutz, S. Prochazka, J. Lorenz, J. Am. Ceram. Soc. 68 (1985) 479.
[7] R.A. Alliegro, L.B. Coffin, J.R. Tinklepaugh, J. Am. Ceram. Soc. 39 (1956) 386.
[8] W. Bröcker, H. Landfermann, H. Hausner, Powder Metall. Int. 11 (1979) 83.
[9] S. Shinozaki, J. Haugas, W.T. Donlon, R.M. Williams, B.N. Juterbock, in: S. Sāmiya (Ed.), Advanced Ceramics II, Elsevier Applied Science, London, 1988, p. 7.
[10] M. Omori, H. Takei, J. Am. Ceram. Soc. 65 (1982) C-92.
[11] M. Omori, H. Takei, U.S. Pat. No. 4502983, 1985.
[12] M. Omori, H. Takei, U.S. Pat. No. 4564490, 1986.
[13] N.P. Padture, B.R. Lawn, J. Am. Ceram. Soc. 75 (1992) 2518.
[14] M.A. Mulla, V.D. Kristic, J. Mater. Sci. 29 (1994) 934.
[15] N.P. Padture, J. Am. Ceram. Soc. 77 (1994) 519.
[16] Y.W. Kim, M. Mitomo, H. Hirotsuru, J. Am. Ceram. Soc. 78 (1995) 3145.
[17] M. Keppeler, H.G. Reichert, J.M. Broadley, G. Thurn, I. Wiedmann, F. Aldinger, J. Eur. Ceram. Soc. 18 (1998) 521.
[18] H. Kodama, T. Miyoshi, J. Am. Ceram. Soc. 75 (1992) 1558.
[19] S.K. Lee, C.H. Kim, J. Am. Ceram. Soc. 77 (1994) 1655.
[20] K. Biswas, G. Rixecker, I. Wiedmann, M. Schweizer, G.S. Upadhyaya, F. Aldinger, Mater. Chem. Phys. 67 (2001) 180.
[21] N. Camuşcu, D.P. Thompson, H. Mandal, J. Eur. Ceram. Soc. 17 (1997) 599.
[22] M.K. Cinibulk, G. Thomas, J. Am. Ceram. Soc. 75 (1992) 2037.
[23] Z. Shen, P. Käll, M. Nygren, J. Mater. Res. 14 (1999) 1462.
[24] A. Rosenflanz, I.W. Chen, J. Eur. Ceram. Soc. 19 (1999) 2325.
[25] K. Hirao, K. Watari, M. Toriyama, S. Kanzaki, J. Am. Ceram. Soc. 84 (2001) 353.
[26] Y. Menke, V. Peltier-Baron, S. Hampshire, J. Non-Cryst. Solids 276 (2000) 145.
[27] T.L. Francis, R.L. Coble, J. Am. Ceram. Soc. 51 (1968) 115.
[28] T.H. Elmer, M.E. Nordberg, J. Am. Ceram. Soc. 50 (1967) 275.
[29] K. Biswas, Doctoral Thesis, University of Stuttgart, 2002.
[30] M. Nader, Doctoral Thesis, University of Stuttgart, 1995.
[31] G.R. Anstis, P. Chantikul, B.R. Lawn, D.B. Marshall, J. Am. Ceram. Soc. 64 (1981) 533.
[32] M. Barsoum, Fundamentals of Ceramics, McGraw-Hill, Singapore, 1997.
[33] L.S. Sigl, H.-J. Kleebe, J. Am. Ceram. Soc. 76 (1993) 773.
[34] W.D. Kingery, J. Appl. Phys. 30 (1959) 301.
[35] A. Rosenflanz, I.W. Chen, J. Eur. Ceram. Soc. 19 (1999) 2325.
[36] H. H. Ye, Doctoral Thesis, University of Stuttgart, 2002.
[37] I. Wiedmann, Doctoral Thesis, University of Stuttgart, 1998.
[38] M. Keppeler, H.G. Reichert, J.M. Broadley, G. Thurn, I. Wiedmann, F. Aldinger, J. Eur. Ceram. Soc. 18 (1998) 521.
[39] Y.W. Kim, M. Mitomo, H. Hirotsuru, J. Am. Ceram. Soc. 80 (1997) 99.
[40] D. Sciti, S. Guicciardi, A. Bellosi, J. Eur. Ceram. Soc. 21 (2001) 621.
[41] S.-L. Hwang, I.-W. Chen, J. Am. Ceram. Soc. 77 (1994) 165.
[42] I.M. Peterson, T.-Y. Tien, J. Am. Ceram. Soc. 78 (1995) 2345.
[43] G. Pezzotti, Acta. Metall. Mater. 41 (1993) 1825.
[44] J. Chen, Q. Tian, A.V. Virkar, J. Am. Ceram. Soc. 75 (1992) 809.
[45] R.W. Rice, C.C. Wu, F. Borchelt, J. Am. Ceram. Soc. 77 (1994) 2539.
[46] D. Chen, M.E. Sixta, X.F. Zhang, L.C. De Jonghe, R.O. Ritche, Acta Mater. 48 (2000) 4599.